

Lightnovo miniRaman spectrometer: Optimal profile for fitting of Raman peaks

Key words

Raman spectrometer; spontaneous Raman spectroscopy; spectral peak; peak fitting; Gaussian profile; Lorentzian profile; Voigt profile.

Introduction

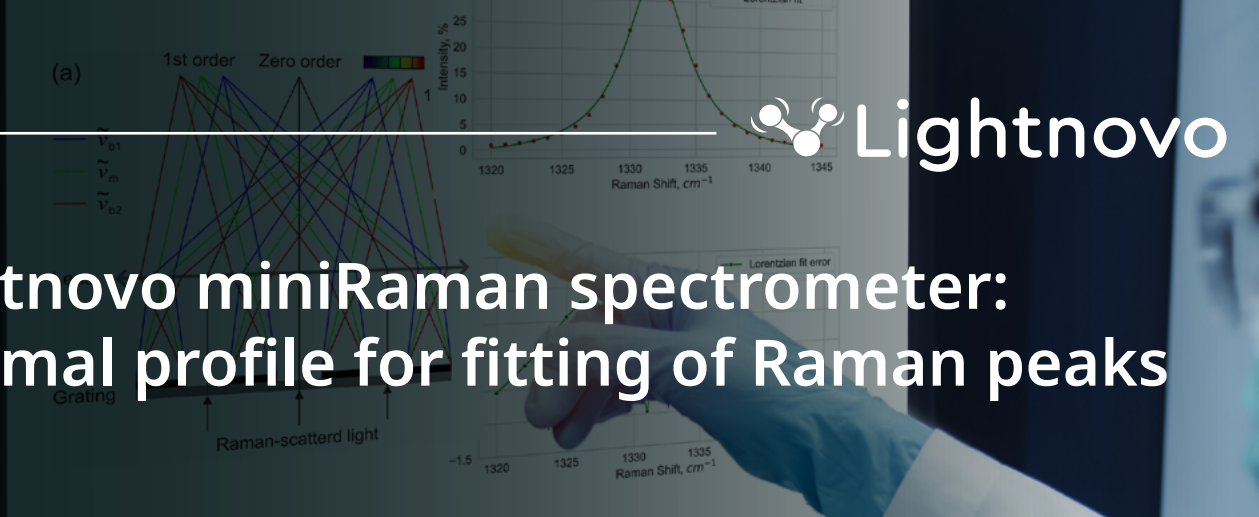
The analysis of spectral peaks is one of the main tasks in Raman spectroscopy [1]. However, a spectrum is typically measured in discrete form, and therefore to accurately characterize a certain peak, it is necessary to first approximate (or fit) its data points with some function (or profile). In the case of symmetrical peaks, which are the most common, the following fitting functions are usually used: Gaussian, Lorentzian, as well as their convolution (Voigt function) or even simple linear combination [1], [2]. At the same time, the peak shape strongly and in a complex manner depends on the features of the measuring equipment. Therefore, for each model of Raman spectrometer, it is advisable to select the best approximation option by experimental verification.

The purpose of this Technical Note is to define a profile type that provides optimal data fitting for symmetric peaks in the spectra measured with miniRaman series spectrometers from Lightnovo [3].

Background

Spontaneous Raman spectroscopy involves exciting (or pumping) the sample by constant-intensity monochromatic light with a suitable wavelength $\lambda=\lambda_p$, and registering the intensity I of the light that it scatters at wavelengths $\lambda\neq\lambda_p$ (inelastic scattering). Typically, the result of such measurements is Raman spectrum – the dependence $I(\tilde{\nu})$, recorded in a certain range of $\tilde{\nu}$, where $\tilde{\nu}=(1/\lambda_p-1/\lambda)$ is so-called Raman shift, expressed in units of $[\text{cm}^{-1}]$.

For Raman-active materials, in the absence (or after the removing) of spurious signals (fluorescence, high-level noises, etc.), the spectrum represents just a set of bands – fragments with some distribution of intensity, which are somehow arranged along the $\tilde{\nu}$ -axis and conditionally isolated from each other, e.g. as in a model spectrum in Fig. 1 (red line). Quite often, in the spectra measured under ambient conditions, almost every band either appears as a single symmetrical bell-like peak (e.g. A and B) or can be represented as a superposition of several such peaks overlapping each other (e.g. band C, which is the sum of the hidden peaks C1 and C2). Asymmetric peaks are less common, and usually occur only for certain substances and/or under specific conditions [2], so they will not be considered here.



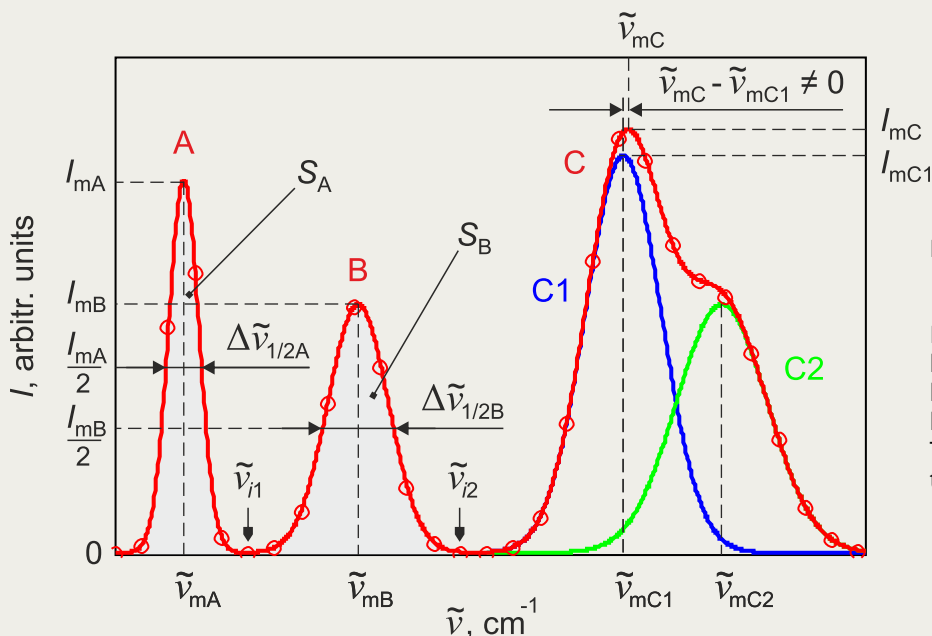


Figure 1. Model Raman spectrum:
 red line – continuous form $I(\tilde{\nu})$;
 red circles – discrete form $I[\tilde{\nu}_i]$.
 Peaks A and B are free-standing, and
 band C results from the overlap of the
 hidden peaks C1 (blue line) and C2
 (green line).
 The notations are explained in the main
 text.

Raman peaks allow to characterize intra- and/or intermolecular bonds of the sample material, or directly evaluate those properties of the sample and/or its environment that are related with these bonds. In so doing, the following peak parameters are typically used: $\tilde{\nu}_m$ – Raman shift at the maximum point (or peak position); $I_m = I(\tilde{\nu}_m)$ – Raman intensity at the same point (or peak height); $\Delta\tilde{\nu}_{1/2}$ – Full Width at Half-Height (FWHH) $I = I_m/2$; S – area under the peak. In Fig. 1 they are supplemented with the peak/band indices.

Strictly speaking, all these parameters can be measured directly only for weakly-overlapping or free-standing peaks, like A and B. As for the hidden ones, it is sometimes possible to estimate a part of the characteristics for certain peaks using the features of the appropriate band. E.g., for C1, the $\tilde{\nu}_0$ and I_0 values can be approximated by the corresponding data for band C, although, as can be seen from Fig. 1, with noticeable errors. Unfortunately, for other hidden peaks, such as C2, the characteristics can't be directly estimated even in this way. Therefore, in general, some preprocessing of the bands is required to deconvolute all hidden peaks.

Raman spectral lines

Fig. 2 (a) illustrates the origin of the spectral lines using a sample consisting of certain identical, non-interacting diatomic molecules as an example. It demonstrates the simplified molecular energy level structure that includes [4]:

- **Electronic levels (quantum number N)** – caused by valence electrons' motion in the fields of atomic cores and their own. The distance between adjacent levels is of the order of several eV.
- **Vibrational levels (V)** – caused by oscillations of atoms in the molecule. The distance between adjacent levels is $\delta E_{vib} \sim 0.1$ eV.

Modern Raman instruments measure the spectrum in discrete form: $I_i[\tilde{\nu}_i] = I(\tilde{\nu}_i)$, $i = 1 \dots M$, where M is the total number of data points, Fig. 1 (red circles). Therefore, to accurately calculate the parameters of a certain discrete free-standing peak, e.g. peak B in Fig. 1: $I_i[\tilde{\nu}_i]$, $i = i_1 \dots i_2$, it is reasonable to use some profile $P(\tilde{\nu})$, which best fits the measured points in the range $\tilde{\nu} \in [\tilde{\nu}_{i_1}; \tilde{\nu}_{i_2}]$. It is obvious that in the ideal case, the equality $P(\tilde{\nu}) = I(\tilde{\nu})$ will be fulfilled on this interval.

The main problem for peak fitting is that the type of the function $I(\tilde{\nu})$, and hence $P(\tilde{\nu})$, is not universal. This is because the actual peak shape is the result of the combined action of several so-called spectral line broadening mechanisms – the processes, which transform a zero-width spectral line into a finite-width peak having certain intensity distribution. Most of this process individually produce a peak with Lorentzian or Gaussian shape, but at the same time each mechanism manifests themselves to varying degree depending on the sample and measurement arrangement/conditions.

- **Rotational levels (J)** – caused by rotations of the molecule and/or her parts. The distance between adjacent levels ~ 0.01 eV.

Thus, each electronic level is splitting into dense substructure of vibrational levels, each of which, in turn, is splitting into even more dense substructure of rotational ones. The essential difference in interlevel distances allows each type of levels to be excited separately by applying light with the appropriate λ_p . This fact is used to implement various types of molecular spectroscopy.

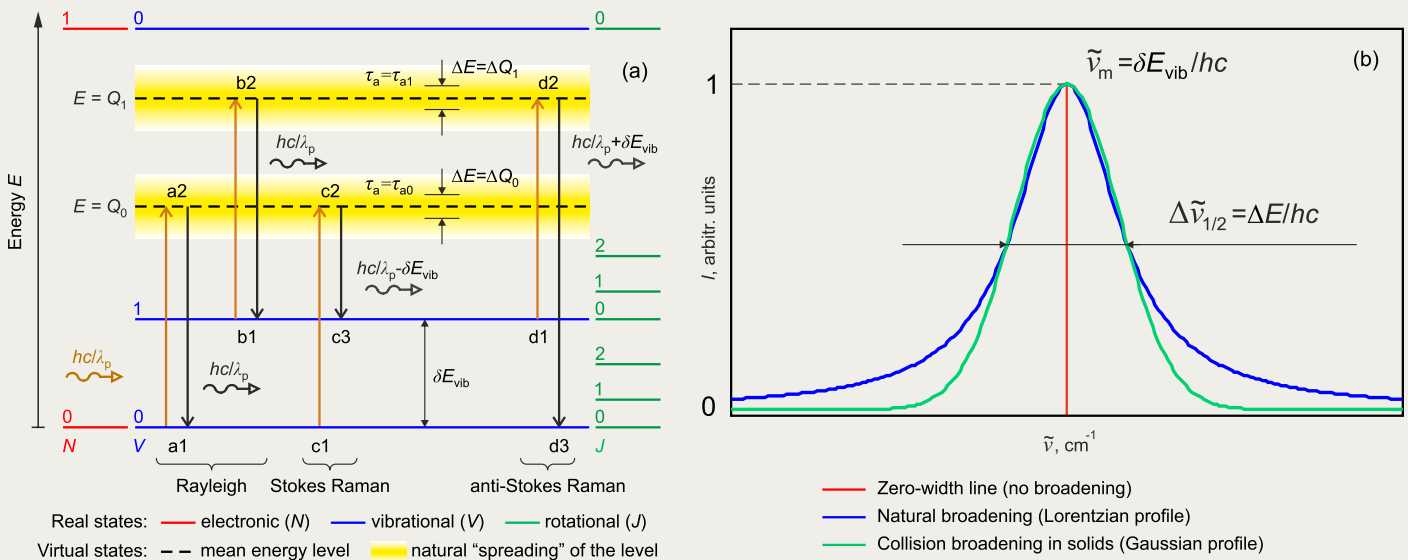


Figure 2. (a) Simplified energy level structure of a diatomic molecule with transitions providing vibrational Rayleigh and Raman scattering. Distances between levels are not shown to scale. (b) Zero-width spectral line and peaks with Lorentzian and Gaussian profiles, resulting from its broadening.

For spontaneous vibrational Raman spectroscopy, λ_p must be such that photons interact with electrons rather than with atoms, but these electrons don't transit from their ground state $N = 0$ to the first excited one $N=1$. In this case, upon absorption of a photon with energy hc/λ_p (where h is Planck's constant; c is speed of light in vacuum), the molecule transits from its ground state $N = V = J = 0$ to the so-called virtual state with energy $E = Q_0$. Besides, it is possible a transition to a virtual state with energy $E = Q_1 = Q_0 + \delta E_{vib}$ from the first excited vibrational state $N = J = 0$, $V = 1$, but under normal conditions the population for this level is significantly lower than the ground one.

The subsequent relaxation provides one of the following vibrational scattering options, which give rise to spectral lines formally having zero width:

- **Rayleigh (elastic) scattering.** The molecule returns to its initial state (transitions $a1 \rightarrow a2 \rightarrow a1$ or $b1 \rightarrow b2 \rightarrow b1$), and emits a photon with energy hc/λ_p equal to the excitation value, thereby providing a spectral line at $\tilde{\nu} = 0$. This scattering type is the most probable and therefore the line has a high intensity. However, for Raman spectroscopy it is usually of no interest.
- **Stokes Raman scattering.** The molecule returns from a virtual state with $E = Q_0$ to the state $N = J = 0$, $V = 1$ (transitions $c1 \rightarrow c2 \rightarrow c3$), and emits a photon $hc/\lambda = hc/\lambda_p - \delta E_{vib}$. The reason for this is the electron-vibrational (or vibronic) coupling, which provides a non-zero probability

that part of the excited-electron energy will be spent on generating a quantum of atomic vibrations. This leads to a spectral line at $\tilde{\nu} = \delta E_{vib}/hc$, Fig 2 (b) (vertical red line), called fundamental. In turn, there is also a probability of returning to one of the states $V > 1$ (not shown in Fig. 2 (a)), giving a line at $\tilde{\nu} = V\delta E_{vib}/hc$, called overtone. Both types of lines allow to found the energy difference between vibrational states, and thus characterize the intermolecular bond. But usually, fundamental line is much more intensive.

- **Anti-Stokes Raman scattering.** The molecule returns from a virtual state with the energy $E = Q_1$ to the ground state $N = V = J = 0$ (transitions $d1 \rightarrow d2 \rightarrow d3$). Here, the electron absorbs a quantum of vibrations due to vibronic coupling, and the molecule emits a photon $hc/\lambda = hc/\lambda_p + \delta E_{vib}$. This gives a line at $\tilde{\nu} = \delta E_{vib}/hc$. But, due to low population for the initial level $N=J=0$, $V=1$ the intensity of this line is weak, which makes it difficult to analyze.

It should be noted that rotational Rayleigh and Raman scattering also occur, generating the corresponding spectral lines. However, their explanation is somewhat more complex [4] and is therefore not considered here. Besides, it is generally accepted that in liquids and solids, rotations are quenched by intermolecular bonds and/or collisions. For this reason, Raman spectroscopy is most often associated just with vibrational scattering.

Spectral line broadening mechanisms

There are quite a lot known reasons for line broadening. The most common are the following [1], [2].

• Natural (or lifetime) broadening

It is a consequence of fundamental quantum effects, and therefore it always occurs, regardless of whether the sample's molecules are free or not, whether they are moving or at rest.

Due to interaction with zero-point vacuum fluctuations, any excited state has a finite lifetime. For virtual states this parameter (usually denoted as τ_a) is very small compared to real ones, and is of the order of several picoseconds [1]. According to the Heisenberg's indeterminacy principle, this gives a large uncertainty in energy: e.g. $\Delta E \geq h/(4\pi\tau_a)$. In other words, each virtual excited level is "spread", as it shown by yellow stripes in Fig. 2(a) for free molecules. The possible energy value for this state follows a certain distribution with mean $E = Q_0$ (or Q_1) and standard deviation $\Delta E = \Delta Q_0$ (or ΔQ_1). Thus, molecules, residing at the same virtual excited state, actually have some differences in energy, and so, upon relaxation, they emit photons with different $\tilde{\nu}$. This broadens the spectral line into a peak whose contour is described by Lorentzian profile, Fig. 2 (b) (blue curve), which obviously reflects the energy distribution for corresponded virtual level of a free molecule.

For this mechanism, the peak's FWHH (often called the natural linewidth) is $\Delta\tilde{\nu}_{1/2} = \Delta E/hc \geq 1/(4\pi c\tau_a)$, so the shorter τ_a , the stronger spectral line broadening will be. In general, τ_a is influenced by which virtual level is occupied upon excitation, i.e. by the energy of incident photons and the distribution of energy states of the molecules. Therefore, $\Delta\tilde{\nu}_{1/2}$ depends on the excitation wavelength λ_p and sample material, and is independent of temperature and pressure, at least until these factors lead to a change in the energy level structure. Anyhow, it is generally accepted that natural broadening is the weakest effect compared to other broadening mechanisms.

• Collision (or pressure) broadening

It is usually considered in coupling with natural broadening. If the sample's molecules don't interact with each other and don't move, a coherence (or correlation) takes place: the molecules, being in a virtual excited state, e.g. with $E = Q_0$ in Fig. 2 (a), are vibrating at the same frequency, defined by their initial vibrational state $V=0$. Then, during Stokes scattering, i.e. the transition to the state $V=1$, due to natural broadening, the spectral peak obtains the smallest (i.e. natural) width and the largest amplitude. Therefore, lifetime τ_a is often called the amplitude correlation time.

However, when molecules interact/collide and move, the coherence is violated: in the virtual state, the vibrational frequencies of some molecules may change (the

so-called dephasing process), so during relaxation they will not transit to the state $V=1$ and contribute to the peak in question, which affect its amplitude/contour. The average time that passes from the moment the molecules came to the virtual excited state until they lose correlation is called the coherence lifetime τ_c . The ratio of τ_a and τ_c affects the resulting peak shape and broadening:

- $\tau_a \gg \tau_c$ – one of the extremes, where dephasing occurs long before relaxation. This applies to gases whose molecules are moving and colliding, but don't bond. Raman peak here is still described by Lorentzian profile, since between collisions the molecules remain free, having the energy distribution for «spreaded» virtual levels similar to that described above.
- $\tau_a \ll \tau_c$ – the opposite extreme, where relaxation occurs long before dephasing. This applies to ideal solids, where molecules/atoms remain in fixed positions. The peak here is close to Gaussian profile, reflecting the distribution of energy states establishing due to strong inter-molecular/atomic bonding. For comparison, this curve is also shown in Fig. 2 (b) as a green line.
- $\tau_a \approx \tau_c$ – the intermediate case, typical for liquids and, in general, for all samples that don't correspond to the first two idealized cases. Accordingly, the resulting spectral peak can be better present by a linear combination of Gaussian and Lorentzian profiles [1], [2].

It is obvious that τ_c decreases with growth of temperature and/or pressure, which intensifies dephasing process and leads to an increase in the peak width $\Delta\tilde{\nu}_{1/2}$.

• Broadening by measuring system

Raman spectrometers have a rather complex design, combining a number of components, which can affect the measured peak's shape. E.g. Fig. 4 shows a general simplified optical scheme of a dispersive Raman spectrometer operating in 180°-backscattering mode. The beam paths illustrate some details of its operation. The parallel monochromatic light beam ($\lambda = \lambda_p$) generated by Laser is focused on Sample using Beam splitter and Lens 1. The last also collimates backscattered light, which further passes through Filter (it only permits Raman-scattered light with $\lambda \neq \lambda_p$) and focused by Lens 2 to Slit. The transmitted light is collimated by Lens 3 and illuminates Grating that spatially disperse this light into range of monochromatic components. Finally, Lens 4 focuses them on Detector, which registers the Raman spectrum in discrete form $I_i[\tilde{\nu}_i]$.

Among the above components, Laser, Grating and Detector usually have the greatest influence in terms of spectral line broadening [2]. Real lasers are not completely monochromatic, but generate light whose intensity is symmetrically distributed with respect

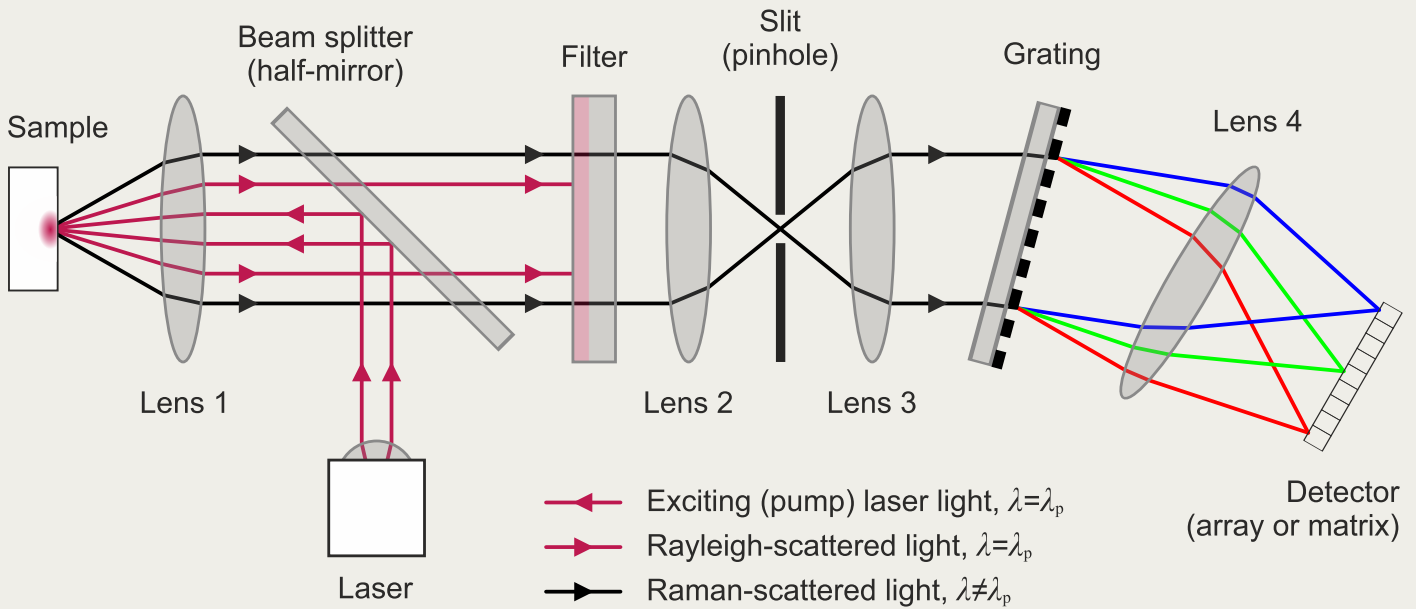


Figure 3. Simplified scheme of dispersive 180°-backscattering Raman spectrometer.

to λ_p over some wavenumber interval, which can be characterized by a certain FWHH value $\Delta\lambda_p$. Typically, this distribution is Gaussian. Therefore, even if other mechanisms are not involved, the spectral line will still be broadened into a peak with Gaussian profile, and, as is easy to show, $\Delta\tilde{\nu}_{1/2} \approx \Delta\lambda_p/\lambda_p^2$. Note that the $\Delta\lambda_p$ value may depend on the spectrometer temperature, power supply, and other factors.

The effects of Grating are illustrated in Fig. 4. Raman-scattered light falls normally on Grating, which forms a diffraction pattern with a non-dispersed zero-order (central) maximum and dispersed higher-orders maxima located symmetrically relative to it. Lens focuses one of the 1st-order maxima on the surface of Detector. Each of its pixels corresponds to a certain $\tilde{\nu}_i$, which allows recording Raman spectrum $I_i[\tilde{\nu}_i]$. For clarity, the “incident” spectrum $I(\tilde{\nu})$ here consists of only one peak at $\tilde{\nu} = \tilde{\nu}_m$, which has vertical boundaries at $\tilde{\nu} = \tilde{\nu}_{b1}$ and $\tilde{\nu}_{b2}$, Fig. 4 (b). For these shifts, the beam paths that form the 1st-order maxima are shown in Fig. 4 (a).

It should be aware that Grating does not simply separate the incident light into monochromatic components. Due to diffraction, each of them also acquires a space, as it shown in Fig. 4 (c) for components with $\tilde{\nu} = \tilde{\nu}_{b1}$, $\tilde{\nu}_m$ and $\tilde{\nu}_{b2}$. Accordingly, in Detector, each such profile will impact several pixels, leading to some measurement errors. In particular, for pixels associated with $\tilde{\nu} = \tilde{\nu}_{b1}$ and $\tilde{\nu}_{b2}$ this leads to general broadening of the measured Raman peak.

Note that broadening effects can also occur from transparent materials of Lenses, Beam splitter or Grating, for example, if their optical properties are strongly wavelength depend.

Ideally, to properly account for the impact of all spectrometer components on Raman peak profile and broadening, it is necessary to determine the corresponding system transfer function. However, this task is, in general, very complex and labor-intensive [5]. Therefore, the most optimal option remains an experimental assessment of the characteristics of the instrument as a whole.

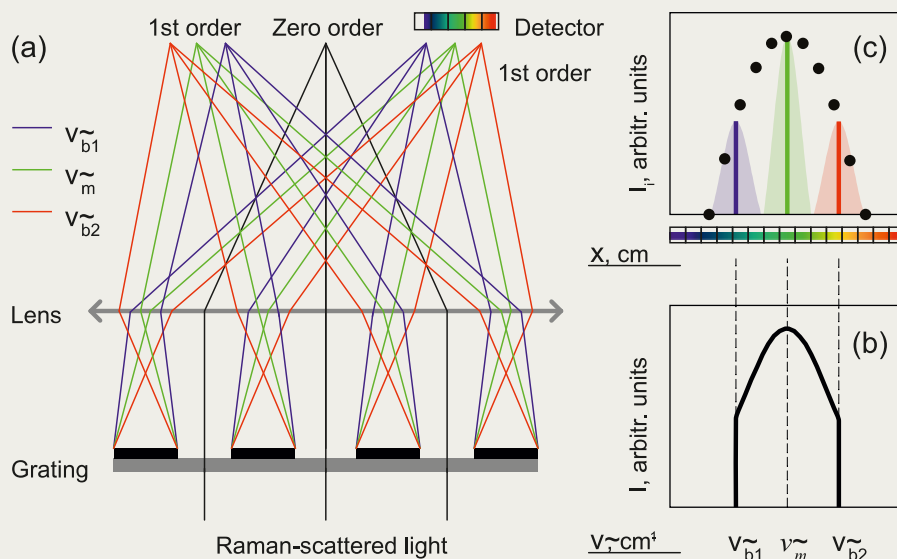


Figure 4. Broadening due to diffraction in spectrometer grating.

(a) Dispersion of Raman-scattered light by a transmission grating.

(b) “Incident” Raman peak.

(c) Measured peak (black dots) and broadening (color profiles) of some its monochromatic components (color lines).



Measuring system: miniRaman spectrometer

The miniRaman is a series of ultra-compact Raman instruments, having the record low sizes ($112 \times 39 \times 34 \text{ mm}^3$) and mass (200 g in aluminum housing). These devices are suitable for most typical applications of Raman spectroscopy, and allow for a variety of use scenarios: the autonomous field hand-held instrument, benchtop instrument, component of a confocal 2D/3D scanning Raman microscope, distant instrument with wireless control etc.

The miniRaman is the dispersive spectrometer that operates in 180° -backscattering mode. The solid-state laser is used to generate light with a wavelength λ_p , which is output to the sample through an entrance lens and a special optical probe (Raman probe). Reflected light is collected by the same components and passes through an entrance slit and an edge filter, which rejects the elastically scattered part of the light having a wavelength λ_p . Then a transmission diffraction grating splits the remaining light into a spectrum, and a CMOS image sensor records them simultaneously across whole instrument's spectral range.

The patented optical scheme of the spectrometer [6] has a number of original solutions and improvements that eliminate the use of expensive, bulky, cooled and moving components significantly reducing the mass-size parameters. At the same time, they made it possible to overcome the main issues inherent in Raman spectrometers, obtain the $\sim 92\%$ throughput from the sample to the detector, effectively decrease the impact of fluorescence on Raman signal, and, as a result, measure the Raman spectrum $I_i[\tilde{\nu}_i]$ with high sensitivity and signal-to-noise ratio.



Figure 5. Lightnovo miniRaman 785 nm spectrometer.

The miniRaman series includes three models: Standard, SERS, and Standard Dual. The first two have a single laser with $\lambda_p = 785 \text{ nm}$ providing the spectral range $\tilde{\nu} = (400 \dots 2700) \text{ cm}^{-1}$. The Dual model has two lasers with $\lambda_p = 785 \text{ nm}$ and 665 nm providing extended spectral range $\tilde{\nu} = (400 \dots 4000) \text{ cm}^{-1}$. All instruments have the same optical scheme with fixed entrance lens, slit, and grating. Different interchangeable Raman probes can be installed to handle various types of samples and/or to arrange required working distances of the instrument.



Sample and measurement procedure

A natural diamond was used as a test sample. This elementary substance is characterized by a simple Raman spectrum with single fundamental peak having a symmetrical shape and a small natural linewidth $\sim 2.5 \text{ cm}^{-1}$ [7]. Its nominal position is $\tilde{\nu}_m = 1332.5 \text{ cm}^{-1}$ [7], however, in the presence of impurities and/or defects, it can be shifted, at least within the range (1331 ... 1333) cm^{-1} [8]. Therewith, this peak is typically of high intensity and free-standing [8].

The measurements were carried out using miniRaman 785 spectrometer ($\lambda_p = 785 \text{ nm}$) equipped with the middle working distance probe [3], which allows the sample to be placed at a distance of 15 mm. The instrument was set to power 112 mW; exposure time 500 ms; and number of repetitions 10. The spectrum $I_i[\tilde{\nu}_i]$ with total number of points $M = 2350$ was measured within the spectral range $\tilde{\nu} = (400 \dots 2750) \text{ cm}^{-1}$.

Data processing

By visual analysis of the measured Raman spectrum, it was identified the above-mentioned diamond's fundamental peak, i.e. the corresponding D data points, $i = 1 \dots D$.

These points were then fitted using three different profiles $P(\tilde{\nu})$ which are based on the functions listed below. All of them have a parameter that determines the position of the maximum ($\tilde{\nu}_m$), as well as the parameters that impact the amplitude and width (γ and σ).

- *Lorentzian function.*

$$f(\tilde{\nu}) = \frac{1}{\pi} \frac{\gamma}{(\tilde{\nu} - \tilde{\nu}_m)^2 + \gamma^2}. \quad (\text{Eq.1})$$

- *Gaussian function.*

$$f_G(\tilde{\nu}) = \frac{1}{\sqrt{2\pi}\sigma} \exp\left[-\frac{(\tilde{\nu} - \tilde{\nu}_m)^2}{2\sigma^2}\right]. \quad (\text{Eq.2})$$

- *Voigt function.* This is the convolution of Lorentzian and Gaussian functions from Eq. (1) and Eq. (2), respectively, defined as:

$$f_V(\tilde{\nu}) = \frac{1}{\sqrt{2\pi}\sigma} \bullet \text{Re}\left[\omega\left(\frac{\tilde{\nu} - \tilde{\nu}_m + j\gamma}{\sqrt{2}\sigma}\right)\right], \quad (\text{Eq.3})$$

- To perform calculations, it is convenient to represent this function in the form:

$$\omega(z) = \exp(-z^2) \left[1 + \frac{2j}{\sqrt{\pi}} \int_0^z \exp(t^2) dt\right], \quad (\text{Eq.4})$$

- where $j = \sqrt{-1}$, and $\omega(z)$ is Faddeeva function of the complex variable $z = \text{Re}(z) + j\text{Im}(z)$. The parameters γ and σ here are inherited from Eq. (1) and in Eq. (2), respectively.

For clarity, the final formula for each fitting profile $P(\tilde{\nu})$ is given below in the corresponding subsection of Results section, along with the relevant table/graph.

The data fitting were performed in Python programming language using *curve_fit* function from *scipy.optimize* package [9]. The Voigt function was implemented through complex number representation utilizing wofz Faddeeva function from *scipy.special* package [9].

In order to assess how closely each profile $P(\tilde{\nu})$ fits the experimental data, it was calculated the difference (error) for each data point of the peak:

$$\Sigma_i[\tilde{\nu}_i] = P(\tilde{\nu}_i) - I_i[\tilde{\nu}_i], \quad (\text{Eq.5})$$

where $\tilde{\nu}_i$ is Raman shift and $I_i[\tilde{\nu}_i]$ is Raman intensity measured at data point number i ($i = 1 \dots D$), and $P(\tilde{\nu}_i)$ is the value of the fitting profile calculated for $\tilde{\nu} = \tilde{\nu}_i$.

Also, in order to compare quantitatively the fitting result for different profiles, it was calculated the root mean squared error (RMSE):

$$RMSE = \sqrt{\frac{1}{D} \sum_{i=1}^D \{P(\tilde{\nu}_i) - I_i[\tilde{\nu}_i]\}^2}. \quad (\text{Eq.6})$$

Finally, for each profile it was numerically measured the main peak parameters: intensity I_m ; position $\tilde{\nu}_m$; and FWHH $\Delta\tilde{\nu}_{1/2}$.



Results

Raman spectrum of diamond

Fig. 6 (a) shows the measured Raman spectrum $I_i [\tilde{\nu}_i]$. Hereinafter, intensity I_i is expressed in a percentage of the saturation level of the CMOS sensor of the spectrometer.

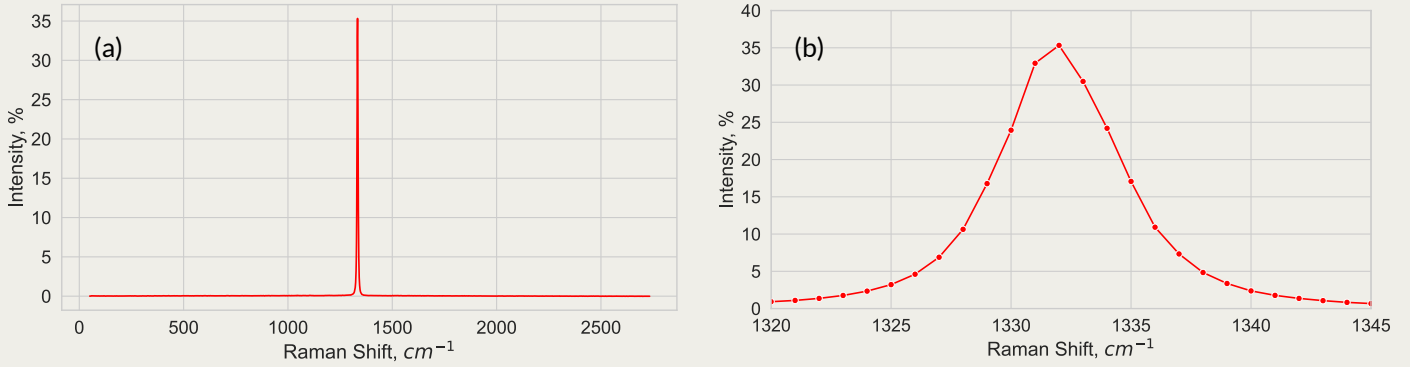


Figure 6. (a) Measured Raman spectrum of a diamond sample. (b) Zoomed region with the fundamental peak, which was used for further data fitting tests.

The spectrum contains only one intense peak, and has virtually no noises and/or other spurious signals in the observed $\tilde{\nu}$ range. This means that the sample has a homogeneous structure with minimal amounts of defects. Since the baseline does not have a noticeable slope, there is no need for special pre-processing of the spectrum. This avoids possible artificial distortions of the curve shape. However, in this case the level of the spectrum's baseline remains non-reduced to

zero. This feature should be taken into account when choosing the profile for peak fitting.

Fig. 6 (b) demonstrates the zoomed fragment of the spectrum in the range $\tilde{\nu} = (1320 \dots 1345) \text{ cm}^{-1}$, which contains the peak of interest, consisting of $D = 26$ data points. Their arrangement is quite symmetrical, which justifies the use of the functions given above for these points approximation.

Fitting with Lorentzian profile

The Lorentzian profile was taken as:

$$P_L(\tilde{\nu}) = A_0 \pi f_L(\tilde{\nu}) + A_1 = \frac{A_0 \gamma}{\gamma^2 + (\tilde{\nu} - \tilde{\nu}_m)^2} + A_1, \quad (\text{Eq.7})$$

where $f_L(\tilde{\nu})$ is Lorentzian function from Eq. (1); A_0 is responsible for true intensity of peak; and A_1 is responsible for its shift along the intensity axis due to the non-zero baseline.

In essence, the fitting procedure consists of automatized finding the coefficient values in Eq. (7) that provide the best agreement between the curve $P_L(\tilde{\nu})$ and the measured points $I_i[\tilde{\nu}_i]$. Table 1 lists the obtained results. In turn, Fig. 7 (a) shows a comparison of Lorentzian profile with the data points, while Fig. 7 (b) demonstrates point-by-point error $\Sigma_i [\tilde{\nu}_i]$ calculated according to Eq. (5).

Table 1. Parameters of Lorentzian profile

Parameter	Value	Parameter	Value
A_0	37.47	γ	2.87
$\tilde{\nu}_m$	1331.97	A_1	-1.65

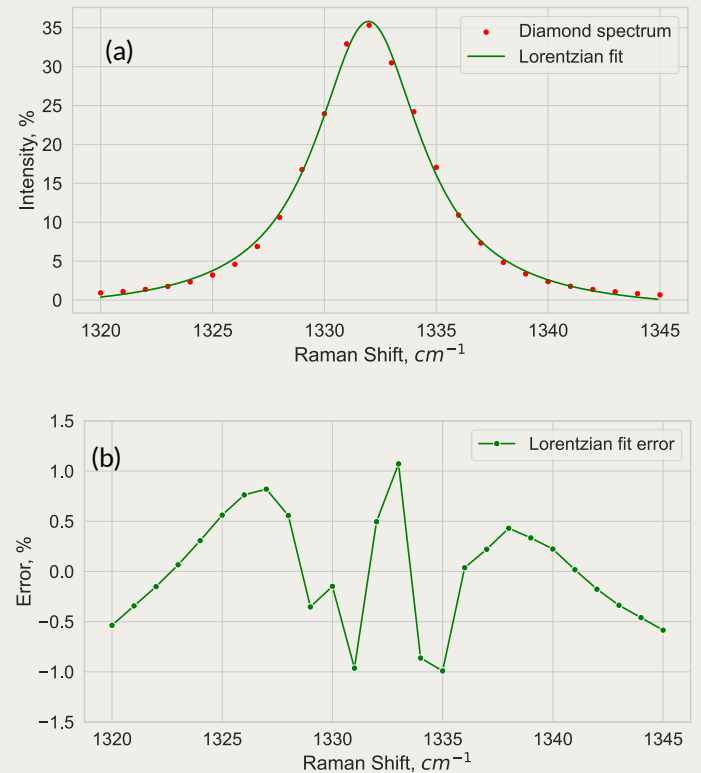


Figure 7. (a) Comparison of Lorentzian profile with the peak's data points. (b) Fit error curve.

Gaussian profile

Gaussian profile was taken in the following form:

$$P_G(\tilde{\nu}) = B_0\sqrt{2\pi}f_G(\tilde{\nu})+B_1 = \frac{B_0}{\sigma} \exp\left[-\frac{(\tilde{\nu}-\tilde{\nu}_m)^2}{2\sigma^2}\right] + B_1, \quad (\text{Eq.8})$$

where $f_G(\tilde{\nu})$ is Gaussian function from Eq. (2); B_0 is the "intensity" and A_1 is the "shift" coefficients.

The curve parameters providing the best data fitting for Gaussian profile are listed in Table 2.

The corresponding curve $P_G(\tilde{\nu})$ together with the measured points $I_i[\tilde{\nu}_i]$ are shown in Fig. 8 (a), while Fig. 8 (b) demonstrates point-by-point error $\Sigma_i[\tilde{\nu}_i]$ calculated according to Eq. (5).

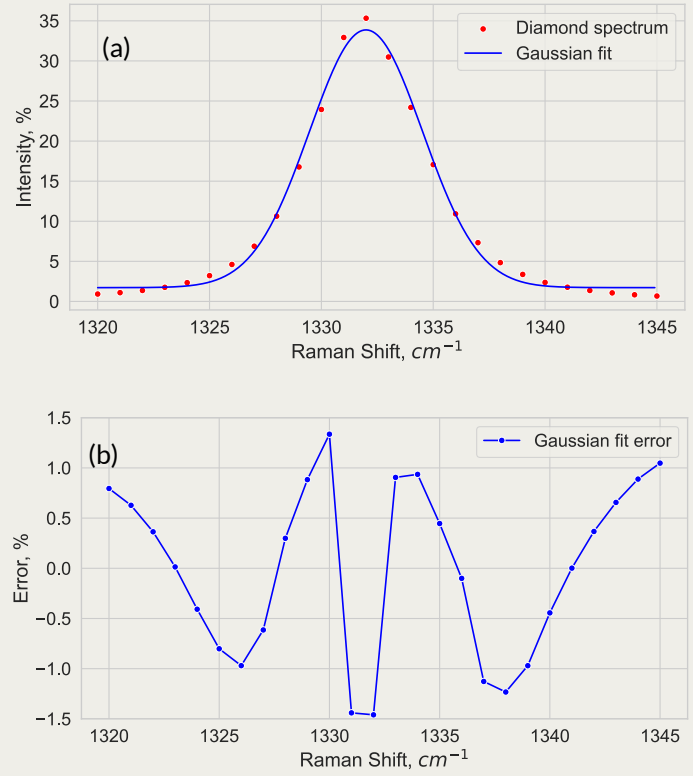


Table 2. Parameters of Gaussian profile

Parameter	Value
B_0	32.15
$\tilde{\nu}_m$	1331.99
σ	2.52
B_1	1.72

Figure 8. (a) Comparison of Gaussian profile with the peak's data points. (b) Fit error curve.

Voigt profile

The used Voigt profile is:

$$P_V(\tilde{\nu}) = C_0f_V(\tilde{\nu}) + C_1 = \frac{C_0}{\sqrt{2\pi\sigma}} \text{Re}\left[\omega\left(\frac{\tilde{\nu}-\tilde{\nu}_m+j\gamma}{\sqrt{2\sigma}}\right)\right] + C_1, \quad (\text{Eq.9})$$

where $f_V(\tilde{\nu})$ is Voigt function from Eq. (3); $\omega(z)$ is Faddeeva function calculated according to Eq. (4); C_0 and C_1 are the "intensity" and "shift" coefficients, respectively.

The best fit is provided by the parameters listed in Table 3. The corresponding curve $P_V(\tilde{\nu})$ together with peak points $I_i[\tilde{\nu}_i]$ are shown in Fig. 9 (a). The point-by-point error curve $\Sigma_i[\tilde{\nu}_i]$ is shown in Fig. 9 (b).

Table 3. Parameters of Voigt profile

Parameter	Value
C_0	292.05
$\tilde{\nu}_m$	1331.98
σ	1.31
γ	2.06
C_1	-0.58

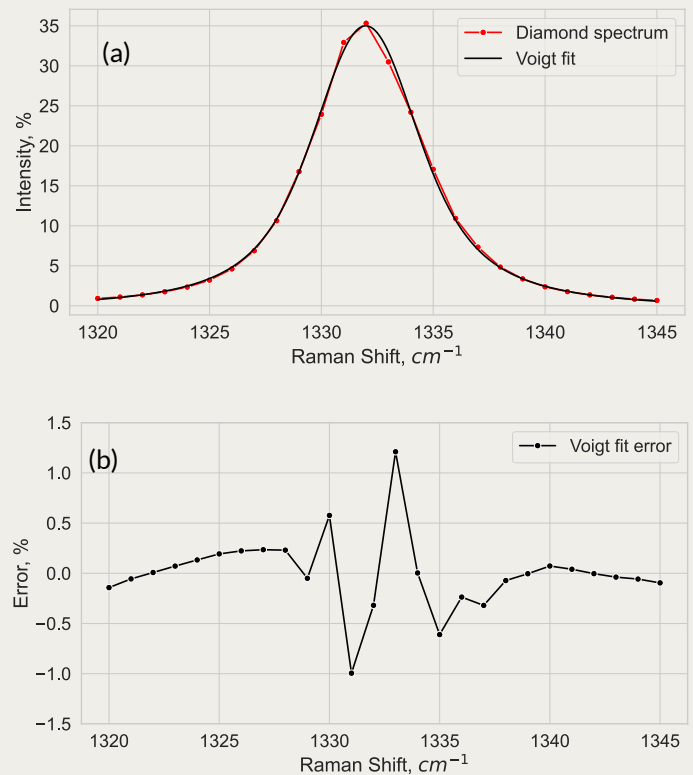


Figure 9. (a) Comparison of Voigt profile with the peak's data points. (b) Fit error curve.

Comparison of different profiles

From the above graphs, it follows that Gaussian profile $P_G(\tilde{\nu})$ is the worst in matching the measured data points. A significant discrepancy is visible to the naked eye in Fig. 8 (a). Besides, this profile exhibits largest errors $\Sigma_i[\tilde{\nu}_i]$ in the central part of the peak, at the edges (or “tails”) and between these regions, Fig. 8 (b).

Lorentzian profile $P_L(\tilde{\nu})$ looks much better visually, Fig. 7 (a), although it still gives quite high fit errors, Fig. 7 (b). Finally, Voigt profile $P_V(\tilde{\nu})$ provides the best fitting, Fig. 9 (a), first of all, at the sides of the peak center, where the values of $\Sigma_i[\tilde{\nu}_i]$ are several times smaller compared to the other two profiles, Fig. 9 (b).

If all three profiles are plotted on one graph, Fig. 10 (a), it is seen that they are quite close each other on the ramps of the central part of the peak. However, in the tail regions, the rate of change of the function for Gaussian profile is too high, while for Lorentzian one it is too low. As a result, they give high fit errors here, but their error curves $\Sigma_i[\tilde{\nu}_i]$ are anti-phased, Fig. 10 (b). The latter fact has a positive effect on Voigt profile: since it is a convolution of Lorentzian and Gaussian functions, their antiphase behavior is mutually compensated, which significantly reduces errors of Voigt fitting in the tail regions, Fig. 10 (b).

Note, that all profiles exhibit the highest fit errors, $\Sigma_i[\tilde{\nu}_i] \sim 1.5\%$, near the peak center, Fig. 10 (b). A possible reason for this is that the peak itself is very narrow and, in the discrete-measured spectrum, its top consists of only three points, which visually have a fairly strong spread. Anyway, it is clean from Fig. 10 (a) that, near the top, Gaussian fit gives underestimated intensity values, while Lorentzian fit, on contrary, leads to somewhat overestimated ones. And again, Voigt fit appears to be the most accurate approximation.

The above reasonings are also supported by the RMSE values calculated for each profile using Eq. (6) and presented in Table 4. Voigt profile has RMSE that is ~ 2.2 and ~ 1.4 times lower than Gaussian and Lorentzian profiles, respectively.

Table 4. Comparison of peak’s characteristics for different profiles

Profile	RMSE, %	$\tilde{\nu}_m, \text{cm}^{-1}$	$\Delta\tilde{\nu}_{1/2}, \text{cm}^{-1}$	$I_m, \%$
Lorentzian	0.54	1331.97	5.74	35.82
Gaussian	0.84	1331.99	5.94	33.86
Voigt	0.38	1331.98	5.82	35.00

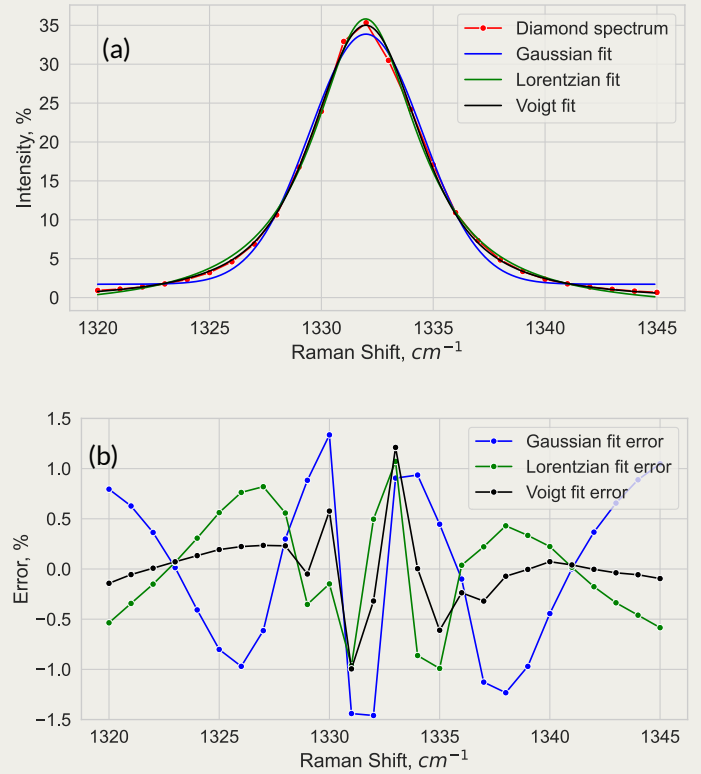


Figure 10. (a) Comparison of Lorentzian, Gaussian and Voigt profiles with the peak’s data points. (b) Comparison of corresponding fit error curves.

Also, Table 4 contains the main peak's characteristics measured for different profiles. All of them give approximately the same peak position $\tilde{\nu}_m \approx 1332 \text{ cm}^{-1}$. This is not surprising, since the original data points as well as the profiles themselves are symmetrical. It is also worth noting that the obtained value $\tilde{\nu}_m$ is in good agreement with the literature data for natural diamond [7] [8].

The FWHH $\Delta\tilde{\nu}_{1/2}$ are vary slightly for different profiles. Therewith, the value measured for Voigt profile, $\Delta\tilde{\nu}_{1/2} \approx 5.82 \text{ cm}^{-1}$, lies, as expected, between the values for Lorentzian and Gaussian profiles. Recall that natural FWHH for natural diamond's fundamental peak is $\sim 2.5 \text{ cm}^{-1}$, but the instrumental broadening observed here is quite consistent with described in [7]. It further demonstrates how strongly the spectrometer can influence the Raman peak width, and highlights the need for experimental evaluation of the measurement performance of each instrument.

Finally, the peak's intensity I_m is perhaps most strongly dependent on the fitting profile. The I_m value for the Voigt profile is between the values for the other two ones. And, as already mentioned, it is this value that best agrees with the measured data.



Conclusion

In general, Voigt profile is suitable function for fitting peaks in Raman spectra measured with Lightnovo miniRaman spectrometers. This type of profile visually matches the measured data points well and provides a low Root Mean Squared Error (RMSE) of fitting. Accordingly, Voigt profile can be used to quantify the main characteristics of Raman peak, such as position, Full-Width at Half-Height (FWHH), intensity, area, etc. At the same time, although Lorentz and Gaussian profiles can be used to determine the position of the peak, but they are poorly suited for assessing its other characteristics, and so their application requires caution.

Measurements carried out on a natural diamond sample showed that the miniRaman spectrometer allows to determine the position of its fundamental peak (1332.5 cm^{-1}) with sufficient accuracy. Therewith, the peak broadening caused by the instrument is not excessive and is quite consistent with the performance of other Raman spectrometers of a similar class.



Literature

1. D. Tuschel, "Peak shape and closely spaced peak convolution in Raman spectra," *Spectroscopy*, vol. 36, no. 9, pp. 10–14, Sep. 2021, doi: 10.56530/spectroscopy.ba4682f3.
2. X. Yuan and R. A. Mayanovic, "An empirical study on Raman peak fitting and its application to Raman quantitative research," *Appl Spectrosc*, vol. 71, no. 10, pp. 2325–2338, Oct. 2017, doi: 10.1177/0003702817721527.
3. "Lightnovo miniRaman spectrometer." Accessed: Oct. 30, 2024. [Online]. Available: <https://lightnovo.com/lightnovo-products/raman-spectrometer/>
4. P. K. Mallick, *Fundamentals of Molecular Spectroscopy*. Singapore: Springer Nature Singapore, 2023. doi: 10.1007/978-981-99-0791-5.
5. Y.-C. Lin and J. V. Sinfield, "Characterization of Raman spectroscopy system transfer functions in intensity, wavelength, and time," *Instruments*, vol. 4, no. 3, p. 22, Aug. 2020, doi: 10.3390/instruments4030022.
6. O. Ilchenko, T. Rindzevicius, A. Boisen, and R. Slipets, "An apparatus for carrying out Raman spectroscopy," WO 2019/145005, Aug. 01, 2019 Accessed: Jan. 29, 2025. [Online]. Available: <https://patentscope.wipo.int/search/en/WO2019145005>
7. G. Morell, O. Quiñones, Y. Díaz, I. M. Vargas, B. R. Weiner, and R. S. Katiyar, "Measurement and analysis of diamond Raman bandwidths," *Diam Relat Mater*, vol. 7, no. 7, pp. 1029–1032, Jul. 1998, doi: 10.1016/S0925-9635(98)00147-2.
8. A. K. Romanovskaya, V. S. Gorelik, D. Bi, and Y. P. Voinov, "Raman scattering in diamond microcrystals and their composites," *J Phys Conf Ser*, vol. 1348, no. 1, p. 012062, Dec. 2019, doi: 10.1088/1742-6596/1348/1/012062.
9. "SciPy API reference." Accessed: Feb. 04, 2025. [Online]. Available: <https://docs.scipy.org/doc/scipy/reference/>

Contact Details

Lightnovo ApS

Blokken 11, 1.

3460 Birkerød

Denmark (DK)

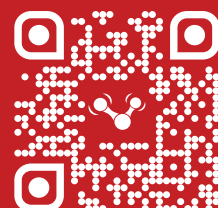
+45 71 37 04 10

info@lightnovo.com

CVR: 40979603

© 2025 Lightnovo ApS. All rights reserved

Scan to learn more about
this and other products



Please consult your local sales
representative for details